PHYSICAL REVIEW B VOLUME 38, NUMBER 2 15 JULY 1988-I

Glancing-angle extended x-ray-absorption fine structure and reflectivity studies of interfacial regions

S. M. Heald, H. Chen, and J. M. Tranquada
Brookhaven National Laboratory, Upton, New York 11973
(Received 24 April 1987; revised manuscript received 9 December 1987)

Glancing-angle extended x-ray-absorption fine structure (EXAFS) and x-ray reflectivity measurements have been made for a Au surface and several Cu/Al interfaces. The Cu/Al samples consisted of 1000 Å Al on Cu, and the measurements demonstrate the potential of these techniques for determining interface structure and morphology. In particular, distinct differences were observed in both the reflectivity and interface EXAFS signals for Cu/Al samples prepared under different conditions. The information obtained on these samples is compared with information obtained by transmission electron microscopy, Rutherford backscattering, and Auger sputter profiling, and excellent agreement is found. The glancing-angle measurements are distorted by anomalous dispersion effects and a simple analytic correction scheme is presented. This correction has been tested on the Au data and found to work well for the entire range of incident angles. For the Cu/Al interfaces the corrections allowed quantitative analysis of the Cu—Al bonding at the interface, and a substantial difference is found for samples prepared under UHV and non-UHV (10^{-6} Torr) conditions. These glancing-angle techniques offer some unique characteristics and are compared to more standard interface studies.

I. INTRODUCTION

A key aspect in understanding interfaces is a determination of their structure and morphology. This paper describes the application of glancing-angle extended x-ray-absorption fine-structure (EXAFS) and x-ray reflectivity measurements to the study of buried interfaces. EXAFS is a well-established probe of the local structure of selected atoms, and has been applied to a wide variety of solid-state systems which diffraction measurements have not been able to fully characterize.[1] In simplified form the EXAFS signal can be written as

$$\chi(k)=\sum_j \frac{N_j}{kR_j^2}B_j(k)\sin[2kR_j+\Phi_j(k)]e^{-2k^2\sigma_j^2} , \quad (1)$$

where the sum is over the neighboring atomic shells. N_j is the number of neighbors in the shell, R_j is their distance and σ_j is the mean-squared deviation in R, k is the photoelectron wave vector, and $B_j(k)$ and $\Phi_j(k)$ are functions characteristic of atoms involved. The backscattering and phase functions are usually calibrated by standards allowing the structural parameters of the first few shells to be extracted. A key advantage is that the lack of long-range order, a situation which often occurs at interfaces, is not a problem. Also, the individual components of an interface can be individually studied by selecting the x-ray energy appropriately.

The main problem in applying EXAFS to interface regions is the separation of bulk and interface signals. One approach is the use of multilayer samples to enhance the interface contribution.[2] In this case separation of interface and bulk contributions often requires the measurement of several samples of varying layer thickness. In this paper it is shown how properties of x rays at glancing angles can be used to confine the x rays to the interface region. When x rays are caused to undergo total external reflection, their penetration into the reflecting surface can be as little as 20–30 Å. Such reflection can be caused to occur at buried interfaces if the substrate is more dense than the overlayer. Thus, by tuning the x-ray energy to an absorption edge of the substrate, the interfacial region can be probed.

The use of glancing angle x rays for structural studies of surface regions was first recognized by Parratt,[3] and a number of authors have used the technique to study such surface regions by EXAFS.[4–8] In most of this work the EXAFS was monitored by measuring the intensity of the reflected beam, although fluorescence detection was shown to have submonolayer sensitivity.[8] This paper describes the application of these techniques to buried interfaces, and extends the brief treatments of this topic presented previously.[9–11]

The paper begins with a detailed description of the optical constants for x rays, and a simple model for calculating their energy dependence. These results will be important for understanding the distortions introduced to the EXAFS by the glancing-angle technique. The x-ray reflectivity is discussed next, as these measurements are used to calibrate the incident angles and provide basic information necessary to characterize the EXAFS distortions. It will also be shown how useful information concerning the interface morphology can be obtained from the reflectivity. Data will be presented for pure Au films and Cu-Al bilayers. The Au films are used to check ideas for correcting the distortions to the EXAFS signal and the Cu-Al data demonstrate the application to a buried interface. In both cases it is demonstrated that the anomalous dispersion distortions can be removed using a relatively simple analytic model, allowing quantitative analysis of the EXAFS to be carried out.

 © 1988 The American Physical Society

II. THE INDEX OF REFRACTION FOR X RAYS

It is conventional to write the index of refraction n in the form[12]

$$n = 1 - \delta - i\beta \ , \tag{2}$$

where both δ and β are positive. The index of refraction is related to the atomic-scattering factor f by the formula

$$n = 1 - 2\pi N r_e \frac{hc^2}{E} \sum_{j=1}^{m} \frac{\rho_j}{A_j} f_j \ , \tag{3}$$

where $r_e = e^2/m_e c^2$ is the classical electron radius and $E = \hbar\omega$ is the x-ray energy. N, the atomic number density, is equal to N_0/A, where N_0 is Avogadro's number, ρ is the mass density, A is the atomic mass, and m is the number of atomic species of the material. If f is written in terms of its real and imaginary parts, $f = f' + if''$, then the quantities δ and β are given by

$$\delta = 2\pi N r_e \frac{hc^2}{E} \sum_{j=1}^{m} \frac{\rho_j}{A_j} f_j' \ , \tag{4}$$

$$\beta = 2\pi N r_e \frac{hc^2}{E} \sum_{j=1}^{m} \frac{\rho_j}{A_j} f_j'' \ . \tag{5}$$

The scattering factor (for forward scattering) for a given type of atom is given by

$$f = Z + \sum_K \Delta f_K \ , \tag{6}$$

where Z is the atomic number and the sum is over absorption edges.

Accurate calculations of scattering factors have been made by Cromer and Liberman,[13] and values at any set of energies can be calculated with their program.[14] However, for model calculations of x-ray reflectivities and correction factors, it is convenient to have a simple analytic formula for calculating f and the index of refraction from limited input information. The sum in Eq. (6) can be broken up into two parts. For the contribution far from their corresponding absorption edges f can be written as $f = f_0' + if_0''$, where $f_0' = Z$ and f_0'' is proportional to the x-ray cross section. For the contribution near the absorption edge under study, anomalous dispersion must be accounted for. One model which can be solved analytically and has been shown to give reasonable agreement with experiment uses a step function (with damping) for the absorption edge, and an E^{-3} dependence for the x-ray cross section above the edge.[12] This gives

$$\Delta f_K = \frac{[x^2 \ln(1 - x^2 + i\kappa x) + x^2 - i\kappa x] g_K}{(x^2 - i\kappa x)^2} \ , \tag{7}$$

where $x = \omega/\omega_K = E/E_K$, g_K is the oscillator strength (see Ref. 12), and $\kappa = \gamma/E_K$ defines the width of the absorption edge. Figure 1 shows the result for δ and $\mu = 4\pi\beta/\lambda$ for copper using this model.

δ and β are also related through Kramers-Kronig relations. If $\beta(\omega)$ is known, then

$$\delta(\omega_0) = \frac{2}{\pi\omega_0^2} \int_0^\infty \frac{\omega^2 \beta(\omega)}{\omega_0^2 - \omega^2} d\omega \ . \tag{8}$$

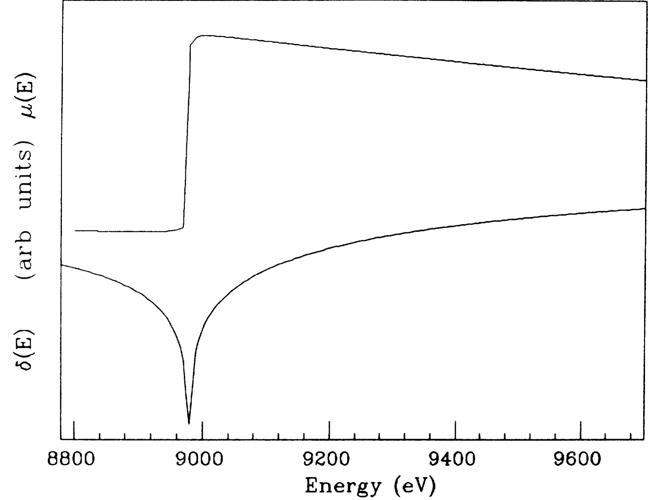

FIG. 1. Calculation of $\delta(E)$ for Cu using the model described in the text and the $\mu(E)$ shown.

Thus, fine structure in $\beta(\omega)$ will influence $\delta(\omega)$. Since an EXAFS experiment measures $\beta(\omega)$, Eq. (8) might appear to be a good way to determine $\delta(\omega)$. However, when using glancing angles the measured signal is not the true absorption coefficient, but includes a contribution from changes in δ with energy. Also, to obtain an accurate value of $\delta(\omega)$, absolute values of $\beta(\omega)$ must be known over a wide energy range, which is not always possible. Restricting the range of the integral in Eq. (8) affects mainly the magnitude of $\delta(\omega)$ rather than any fine structure, and, ignoring this systematic error, we have used the Kramers-Kronig relation to compare the relative phases of the fine structure in $\delta(\omega)$ and $\beta(\omega)$. Figure 2 shows an example for Cu near the K edge. In agreement with other authors,[15,16] the structure in $\delta(\omega)$ is found to be $\sim\pi/2$ out of phase with the EXAFS in $\mu(\omega)$.

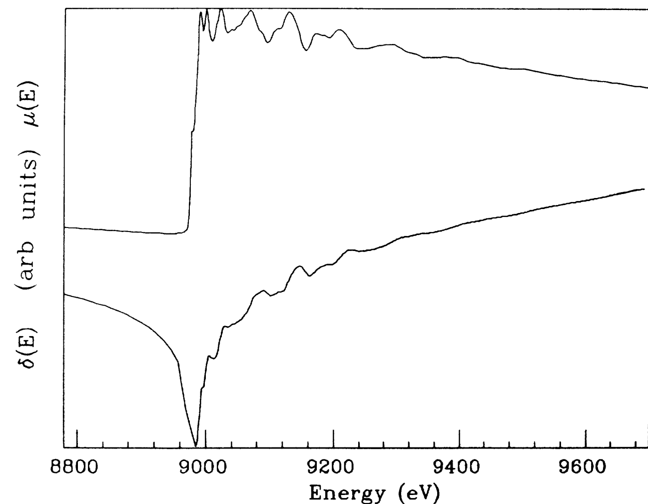

FIG. 2. Calculation of $\delta(E)$ for Cu using a Kramers-Kronig analysis of the $\mu(E)$ data shown.

III. REFLECTION OF X RAYS

Once the optical constants have been determined, the x-ray reflectivity can be calculated using the Fresnel equation:[3]

$$\frac{I_R}{I_0}=\frac{h-(\theta/\theta_c)[2(h-1)]^{1/2}}{h+(\theta/\theta_c)[2(h-1)]^{1/2}}\ , \tag{9}$$

where

$$h=\left[\frac{\theta}{\theta_c}\right]^2+\left\{\left[\left[\frac{\theta}{\theta_c}\right]^2-1\right]^2+\left[\frac{\beta}{\delta}\right]^2\right\}^{1/2}\ , \tag{10}$$

and $\theta_c=\sqrt{2\delta}$ is the critical angle below which total external reflection occurs. Equation (9) applies to a single homogeneous layer. When multiple layers are involved, the surface reflectivity can be related to the reflectivity of deeper interfaces through a recursion relation. The calculation can then proceed up from the semi-infinite bottom layer for which one has the boundary condition that the amplitude of the reflected ray is 0.

A number of essentially equivalent methods exist for treating the multiple-layer case. We have chosen to use the matrix formalism of Vidal and Vincent.[17] Included in this calculation is the possibility for interface roughness. They assume that the probability of finding a point on the interface at a particular value z (the reflecting surface is in the $x-y$ plane) is Gaussian:

$$W(z)=(2\pi\gamma^2)^{-1/2}\exp[(z-z_0)^2/2\gamma^2]\ . \tag{11}$$

This model assumes that the roughness parameter γ is much less than the layer thickness and that the roughnesses of the interfaces are uncorrelated. When the roughness is large ($\gamma > 50$ Å) it has been found preferable to treat the interface as a succession of thin layers with gradually varying density. Both of these models are scalar in that they do not depend on the form of the roughness in the x-y plane.[18]

Figure 3 compares the calculated reflectivity for a bilayer system of 1000 Å of Al on a Cu substrate with the reflectivity of pure Al and Cu surfaces. Of interest here is the region above the Al critical angle and below the Cu critical angle. In the bilayer case the x rays are reflecting from the interface, and strong interference oscillations appear as the optical path in the overlying Al layer is changed by varying the angle. For interface sensitivity the important parameter is the penetration of the x rays into the Cu substrate. To evaluate the sensitivity of glancing-angle x-ray-absorption measurements to the interface region, a model calculation was performed on a trilayer system consisting of a 1000-Å Al/50-Å $CuAl_2$/Cu substrate. The results for the penetration depth of the x rays past the Al/$CuAl_2$ interface as well as the relative Cu fluorescence signals from $CuAl_2$ and Cu are shown in Fig. 4. The sensitivity of the technique is illustrated by the dominance of the $CuAl_2$ fluorescence signal at small angles, even though the Cu density in $CuAl_2$ is only 0.28 that of pure Cu.

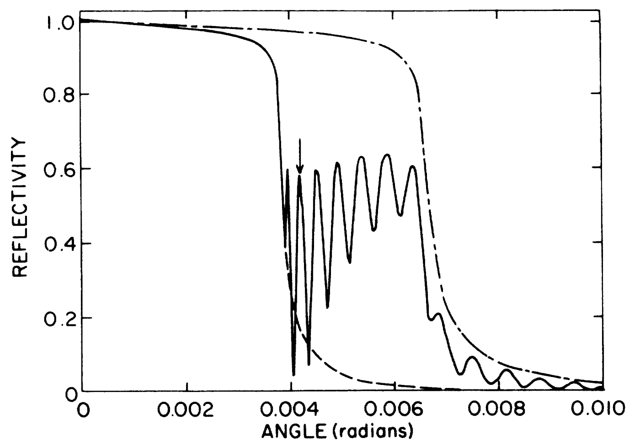

FIG. 3. Calculated reflectivity for pure Al (dashed line), pure Cu (dotted-dashed line), and 1000 Å of Al on Cu (solid line) at 8.6 keV.

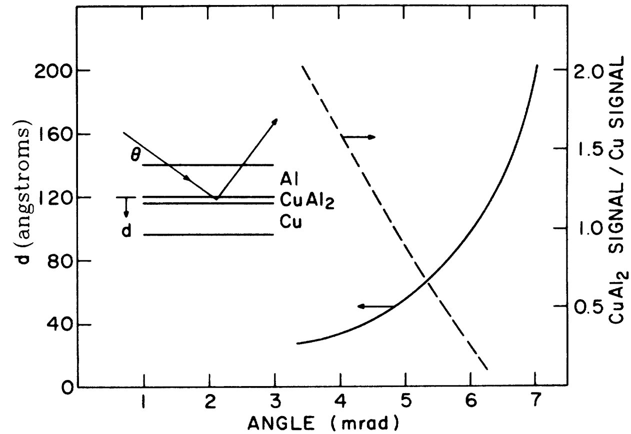

FIG. 4. Solid line: Calculation of the penetration of the incident x rays below the Al-$CuAl_2$ interface for a model system of 1000-Å Al/50-Å $CuAl_2$/1000 Å Cu at an x-ray energy of 9.3 keV. Dashed line: Calculation of the relative contribution to the Cu fluorescence signal of the Cu and $CuAl_2$ layers.

These results indicate that interface layers as thin as 10 Å should be easily detectable in the fluorescence signal if the interface roughness is small. As the roughness increases, the x rays are not as sharply confined to the interface regions and the sensitivity decreases. The amplitude of the interference oscillations in the reflectivity is sensitive to the roughness and, thus, analysis of the reflectivity signal is essential in determining the region being probed by a glancing-angle EXAFS measurement.

IV. EXPERIMENT

Figure 5 shows the basic experimental geometry. The incident beam is collimated by a fine slit (~50–100 μm) and is monitored by an ionization chamber. The sample is mounted on a stepping-motor-controlled angle stage with a step resolution of 0.3 seconds of arc. The stage and slit are aligned parallel to each other to ~30 seconds of arc. Simultaneous measurement of the reflected and fluorescence signals is accomplished using ionization

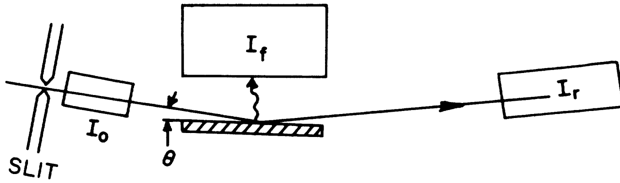

FIG. 5. Experimental setup for glancing-angle reflectivity and fluorescence measurements.

chambers. The large-area fluorescence detector is situated to collect a solid angle of $\sim\pi$ steradians.

The measurements were performed at the Cornell High Energy Synchrotron Source (CHESS) beamline C-2 and the National Synchrotron Light Source (NSLS) on beamline X-11A. In both cases the x-ray flux incident on the sample is $(1-5)\times 10^8$ photons/s and the fluorescence signal is in the range $(1-10)\times 10^6$ photons/s. Thus, an individual EXAFS scan could be completed in ~ 15 min.

A number of samples have been measured. In this paper we will concentrate on two systems: pure Au and Al on Cu prepared under varying conditions. All were deposited onto float-glass substrates (2.5×5 cm^2). The Au sample and one of the Cu-Al samples were prepared by evaporation in a chamber with a base pressure of $\simeq 10^{-6}$ Torr. A thin Cr layer was deposited first to aid adhesion to the substrate. For an unreactive element such as Au, such a base pressure should have little effect on the film composition. For the Al-on-Cu sample, however, incorporation of impurities into the layers is likely at 10^{-6} Torr. Therefore, two other samples were prepared: one by evaporation in a chamber with a base pressure of 5×10^{-10} Torr, and one by sputtering in a chamber with a base pressure of 2×10^{-7} Torr.

The Au sample was characterized by optical profilometry to have a surface roughness of 6 Å rms. This is the expected value for a float-glass substrate. The Al/Cu samples were characterized by cross-sectional transmission electron microscope (TEM). For the sample evaporated at 10^{-6} Torr the Cu/Al interface and Al surface were both observed to be distinctly rougher than the substrate. This is seen in Fig. 6(a). For preparing the TEM samples it was necessary to use a silicon wafer as a substrate. These have roughness similar to float glass and should not significantly change the interface or surface roughness. From the micrograph it is seen that the peak-to-peak roughness of both the interface and surface is in the range 50–100 Å. The sputtered sample is shown in Fig. 6(b). In this case the roughness is distinctly larger and it is difficult to clearly identify the interface. A rough estimate based on this and other micrographs is a peak-to-peak roughness of ~ 500 Å.

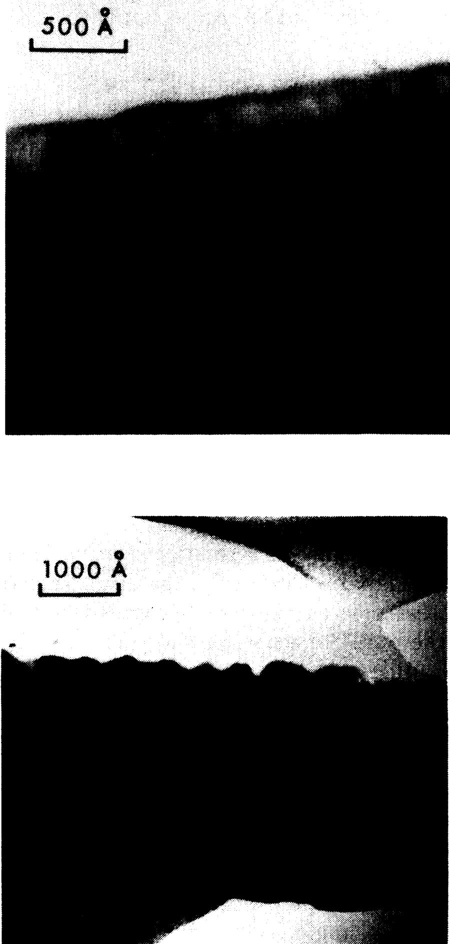

FIG. 6. Cross-sectional TEM photographs of (a) evaporated Al/Cu bilayer, and (b) sputtered Al/Cu bilayer.

V. REFLECTIVITY DATA

Reflectivity data are obtained by fixing the incident energy and scanning the angle stage. A brief discussion is given here as it applies to understanding the EXAFS results to follow. Typically, the reflectivity is measured above and below the absorption edge at energies well away from the anomalous dispersion region. Figure 7 shows the x-ray reflectivity for the Al/Cu sample evaporated at 10^{-6} Torr. These are integrated reflectivity measurements as there was no exit slit before the I_r detector, and both the specularly reflected beam and any nearby scattered radiation is detected. Photographs of the reflected beam showed it to be very clean, with little scattered radiation outside the specularly reflected beam.

Excellent fits to the data could be obtained using the Fresnel equation modified for roughness as described in Sec. III. The fits were carried out in two stages. First, the low-angle regions of the two scans are fitted separately to determine the zero offset and overall normalization factors. This region is relatively insensitive to structural parameters. Then, the two scans are simultaneously fitted to determine the structural parameters. Such simultaneous fitting of different energies improves the sensitivity to the element whose absorption edge is crossed, in this case Cu. Included in the fits was a thin (20 Å) Al_2O_3 layer at the surface, although the determined roughness value of $\gamma=26$ Å cannot be taken too seriously since it is larger than the film thickness and out-

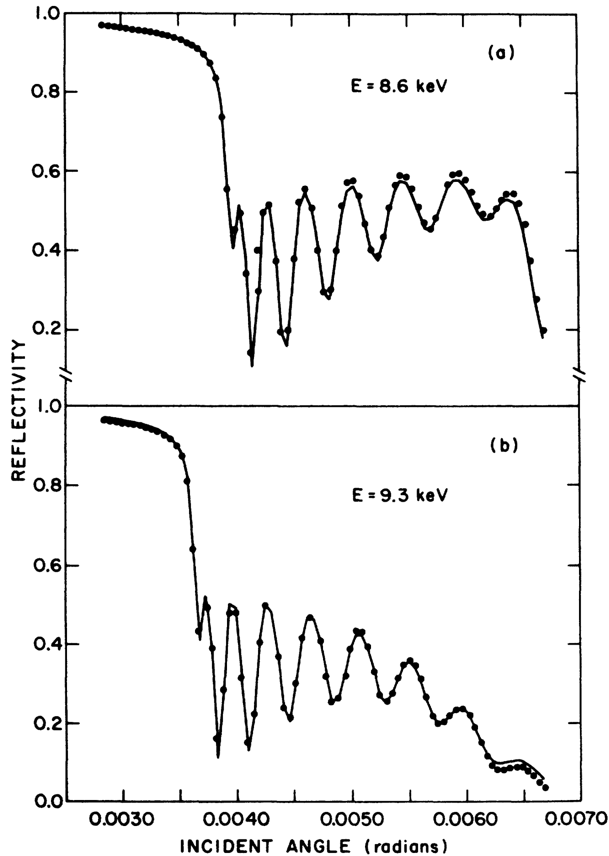

FIG. 7. Comparison of the fit described in the text (solid line) with the experimental reflectivity data (points) for the evaporated Al/Cu sample. The fitting parameters are as follows: Al_2O_3, $d=20$ (fixed), $\gamma=26$; Al, $d=976$, $\gamma=25$; Cu, $d=1000$ (fixed), $\gamma=23$, where d is the layer thickness and γ is the roughness (in Å). Also, the Al layer had 0.7 at. % Cu included.

side the range of validity for the roughness model. Sputter profiling of Al surfaces prepared similarly to the samples gave an Al_2O_3 thickness of ~ 15 Å.

The reflectivity data are very sensitive to the Al thickness, which determines the oscillation frequency. The error in thickness determination is estimated to be $\sim 1\%$. The Cu thickness was not important since in the angle-range fit the x rays are not penetrating the Cu layer. The roughness parameters for the Al and Cu layers are both around 25 Å. Since these are 1σ values, they are in good qualitative agreement with the larger peak-to-peak values seen in the electron micrographs. Quantitative values obviously depend on the structural model employed to calculate the roughness. The fits are also improved by including about 0.7 at. % Cu in the Al layer. Auger sputter profiling of the film did seem to indicate a small amount of Cu in the Al layer, possibly due to grain-boundary diffusion. However, for concentrations at this level, it is also possible the Cu additions are compensating for inaccuracies in the Al optical constants. Such small concentrations appear to be near the limit of our sensitivity for reflectivity measurements alone. Analysis of the EXAFS data discussed in Sec. VII also confirms the presence of Cu in the Al layer.

At angles just above the Al critical angle the two reflectivity curves are quite similar. This is a consequence of the small penetration into the Cu layer. As the angle is increased, the penetration increases and larger absorption above the Cu edge increasingly attenuates the reflected signal.

Fitting of the Au reflectivity was much simpler since only the surface parameters were important. In this case the roughness was found to be $\gamma=13\pm2$ Å. The disagreement of this result with the profilometer result of 6 Å is not surprising since the optical measurement averages over $\sim 1\ \mu m^2$ areas, and does not detect finer-scale roughness.

As might be expected from the TEM results, fitting of the reflectivity from the sputtered sample was more difficult. A number of models were tried, all of which gave qualitative agreement, but none were entirely satisfactory. Since this paper is concentrating on the EXAFS results, a more detailed discussion of these fits will be published later. It is important, however, to note that analysis of the reflectivity is important for a complete understanding of the EXAFS results. Interface roughness affects the penetration of the x rays, which determines the region that the EXAFS results apply to.

VI. EXAFS RESULTS

As mentioned, EXAFS measurements were made by detecting both the fluorescence and reflected signals as the incident energy is scanned. Previous authors have generally analyzed the reflectivity signal,[4–7] but in the present study the signal-to-noise ratio of the fluorescence signal was found to be superior in almost every case. This may seem surprising since the reflected beam intensity is substantially higher than the fluorescence. However, in most cases, the signal-to-noise ratio in the data was not dominated by statistics. It appears that small fluctuations of the beam position or angle cause much of the noise. These affect the total intensity of both the reflected and fluorescence signal. The edge step in fluorescence is, however, a much larger fraction of the total intensity, resulting in a smaller relative fluctuation in the EXAFS signal. Obviously, the advantage of fluorescence increases as the system becomes more dilute, but even for the pure Au data the fluorescence data were superior. In this case the reflectivity decreased 20% in crossing the edge, while the change in the fluorescence signal was several times the background. Thus, the effects of beam fluctuations were enhanced $\sim 5\times$ in the reflectivity data.

Figure 8 illustrates another problem present in both the fluorescence and reflectivity signals when bilayer samples are measured. As the incident energy is changed, the critical angle is changed, and the effect is similar to varying the incident angle. Thus the reflectivity oscillations appear in both EXAFS signals. The fluorescence signal depends on the interface intensity and the penetration depth of the x rays. Since away from θ_c the penetration

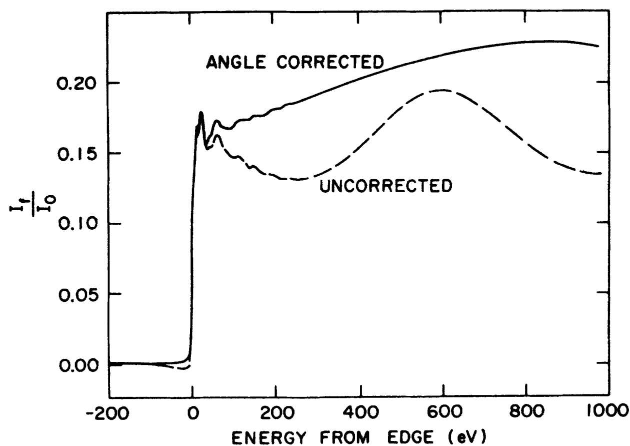

FIG. 8. The fluorescence signal at the Cu K edge (8.980 keV) for the evaporated sample at 4.0 mrad incident angle. In the uncorrected case the change in critical angle with energy causes large changes in reflectivity (see Fig. 7) which give corresponding changes in the fluorescence. These are nearly eliminated when the angle and energy are scanned simultaneously.

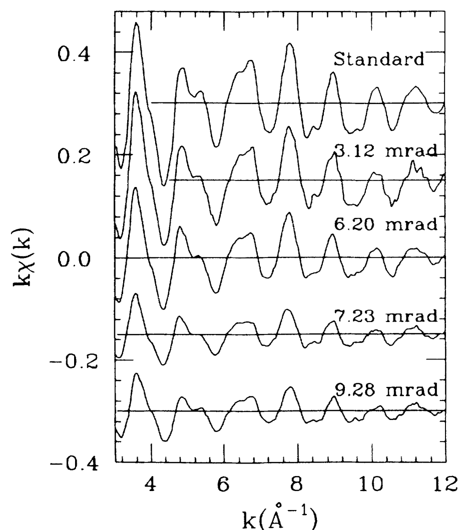

FIG. 9. Variation in the EXAFS $X(k)$ for Au as a function of incident angle.

depth is a slow function of the angle, the change in fluorescence signal is a measure of the interface intensity. This is generally smaller than the change in reflectivity since the reflectivity also depends strongly on absorption in the top layer. As seen in Fig. 8, the fluctuations are a significant fraction of the fluorescence signal. The modulations in the reflectivity are even larger, as can be seen from the magnitude of the oscillations near 4 mrad in Fig. 7.

Figure 8 also shows the solution to this problem. As the energy is scanned the incident angle is varied to compensate for the change in critical angle. The critical angle varies as $1/E$ away from the edge. Thus, the correction used was

$$\theta=\left[1-\frac{\Delta E}{E}\right]\theta_0 , \quad (12)$$

where E and θ_0 are the initial values. The correction was carried out in two ways: using a piezoelectric translator (PZT) with a total range of 0.6 mrad or by stepping the angle-stage motor. The PZT had some nonlinearity which resulted in the residual curvature seen in the corrected curve in Fig. 8. This was not a serious problem. At higher angles the available range from the PZT was inadequate and the motor correction was used.

A. Au data

EXAFS spectra for Au at various incident angles are shown in Fig. 9. As the angle is increased the distortion in the spectra increases. These measurements were all made under ambient conditions at room temperature. Therefore, the samples are all expected to have a thin adsorbed layer of low-z material. An advantage of Au is that it is unreactive and the local surface structure should be essentially identical to bulk Au. At the x-ray energies and angles used this adsorbed layer should have a negligible affect on the measurements. There is a possible distortion of the surface layer of atoms, and calculations indicate this layer could be contributing as much as 10% of the fluorescence signal at low angles. For the present work the x-ray polarization is oriented in the plane of the sample, minimizing the contribution to the EXAFS of an adsorbed layer. Thus, the measurements in Fig. 9 should provide a good measure of the distortions caused by the glancing-angle technique.

B. Cu-Al Data

An extensive set of EXAFS measurements as a function of annealing temperature and incident angle have been taken. In this paper only the unannealed samples are analyzed to demonstrate the sensitivity of the technique. A more extensive discussion of the Cu-Al annealing results will be the subject of a forthcoming paper.

EXAFS spectra for the Cu-Al samples are shown in Fig. 10. Since these data are not yet corrected for the glancing-angle distortion, the amplitude of the Cu standard spectra has been arbitrarily multiplied by $\frac{1}{2}$ to make comparison easier. Even in uncorrected form, it is clear that there are distinct differences in the interface EXAFS for the differing preparation conditions. For the sample evaporated at 10^{-6} Torr the EXAFS is nearly identical to the Cu standard, indicating an almost unreacted interface. Both the sputtered sample and the UHV evaporated samples show substantial differences from bulk Cu, especially at low k, where the signal from Cu—Al bonds should be the strongest. $CuAl_2$ is the first phase observed to form at the interface with thermal annealing.[19,20] The temperatures of the samples during deposition are estimated to be less than $\sim 50\,^{\circ}C$, well below the temperature required for annealing. Thus, the presence of Cu—Al bonds seem to be due to the deposition process.

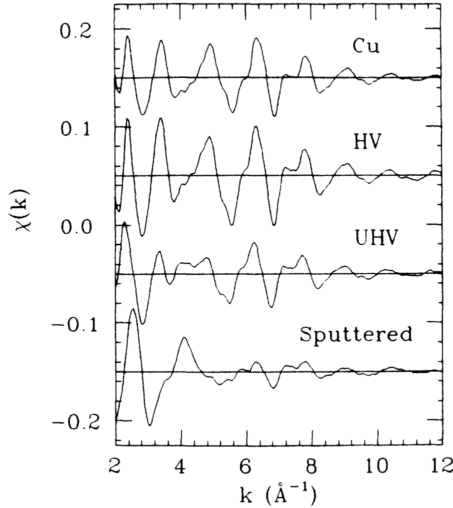

FIG. 10. Comparison of uncorrected EXAFS obtained for a Cu/Al interface prepared by evaporation at 10^{-6} Torr (HV), at 5×10^{-10} Torr (UHV), and by sputtering. The incident angle was about 4.6 mrad for each. For comparison the EXAFS from a Cu foil multiplied by 0.5 is shown.

In Fig. 11 the data from the UHV sample at different incidence angles are used to demonstrate the controllable penetration depth with angle. As will be discussed in Sec. VIII, the Cu-Al intermixed region in this sample is estimated to be 40 Å thick. It is seen that for angles just above the Al critical angle there is a strong enhancement of the Cu-Al component of the signal. As the angle is increased, the penetration into the Cu substrate increases, and the signal clearly becomes more Cu-like. Comparison with the $CuAl_2$ standard indicated that the Cu—Al bonding is quite similar to $CuAl_2$ since a linear sum of Cu and $CuAl_2$ reproduces the major features of the interface spectra. However, before a detailed comparison can be made, the anomalous dispersion distortions must be removed. This is the subject of the next section.

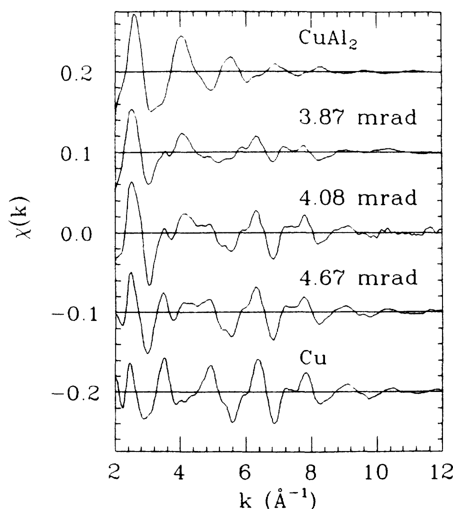

FIG. 11. The angular dependence of the uncorrected interface EXAFS for the UHV evaporated sample. For comparison, the Cu and $CuAl_2$ spectra are shown multiplied by 0.5.

VII. ANOMALOUS DISPERSION CORRECTIONS AND DATA ANALYSIS

As the data in the preceding section demonstrate, in many cases useful information can be gained from the glancing-angle EXAFS spectra in spite of the anomalous dispersion distortions. To analyze the data more quantitatively, however, and to understand more fully the limitations of the technique, it is necessary to look more closely at the distortions.

The fluorescence intensity can be written as

$$I_f=\mu F(\beta,\delta)\ , \tag{13}$$

where F is the integral of the x-ray intensity as a function of depth into the sample and μ is the absorption coefficient of the element being measured. If F were energy independent, then the EXAFS would be undistorted. In certain cases, such as when the incident angle is very small or when μ is due to a dilute component, this is almost the case. For other situations we note that $\mu=\mu_0+\chi$, where μ_0 is the smooth part of the absorption as shown in Fig. 1 and χ is the small contribution due to the EXAFS. Thus, I_f can be expanded and to first order in χ,

$$I_f=\mu_0F_0+\mu_0\chi\frac{dF}{d\mu}+\chi F_0\ , \tag{14}$$

where $F_0=F(\beta_0,\delta_0)$ refers to the smooth part of F (calculated from β and δ without the superimposed EXAFS oscillations). Collecting terms and expanding the derivative, this can be written as

$$\frac{I_f}{F_0}=\mu_0+\chi\left[1+\frac{\beta_0}{F_0}\frac{\partial F}{\partial\beta}+\frac{\beta_0}{F_0}\frac{\partial F}{\partial\delta}\frac{d\delta}{d\beta}\right]\ , \tag{15}$$

where the term in parentheses gives the distortion in χ. All of these terms can be calculated using the simple analytic model given in Sec. II for δ_0 and β_0, except for the phase of $d\delta/d\beta$.

The derivative $d\delta/d\beta$ must be treated as complex since the oscillations in δ and β are out of phase. If we write

$$\frac{d\delta}{d\beta}=\left|\frac{d\delta}{d\beta}\right|e^{i\phi}\ , \tag{16}$$

then the analytic model can be used to determine the magnitude. From Eq. (7) the magnitude is given by $\mathrm{Re}(\Delta f_K)/\mathrm{Im}(\Delta f_K)$. A Kramers-Kronig analysis is required to determine the phase. This might seem to contradict the goal of avoiding a Kramers-Kronig analysis to determine δ. However, in this case only the phase is required which minimizes the importance of truncation of the integral range, and does not require absolute values of β to be determined. Also, the phase is not strongly dependent on the material being studied. Martens and Rabe[5] concluded on the basis of model calculations that $\phi=90°\pm5°$ for all cases. Our Kramers-Kronig analysis of experimental Cu and Au data is essentially in agreement, with $\phi=75°-80°$. Thus, it is not necessary to determine the phase for every data set.

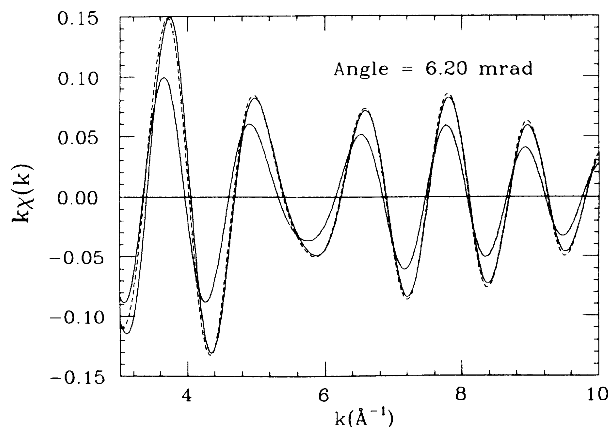

FIG. 12. Corrected and uncorrected EXAFS $\chi(k)$ for Au at 6.20 mrad incident angle (solid curves) compared to the spectra from pure Au (dashed line).

Using Eqs. (15) and (16), the correction factor can be broken up into its amplitude ($\mathcal{A}$) and phase ($\mathcal{P}$) components:

$$\mathcal{A}=[C_\beta^2+C_\delta^2+2C_\beta C_\delta\cos(\phi)]^{1/2} ,$$
$$\mathcal{P}=\tan^{-1}\{C_\delta\sin(\phi)/[C_\beta+C_\delta\cos(\phi)]\} , \tag{17}$$

where

$$C_\beta=1+\frac{\beta_0}{F_0}\frac{\partial F}{\partial\beta} , \quad C_\delta=\frac{\beta_0}{F_0}\frac{\partial F}{\partial\delta}\left|\frac{d\delta}{d\beta}\right| . \tag{18}$$

These corrections can be applied to the amplitude and phase factors $B(k)$ and $\Phi(k)$ in Eq. (1).

We now summarize the correction procedure: First, the reflectivity is analyzed to generate a model for calculating $F(\beta,\delta)$. Then, the fluorescence data are divided by F_0 and analyzed in the usual fashion to extract the EXAFS, χ. This χ has distortions which are corrected by applying Eqs. (17) to the amplitude and phase. All of the steps employ the analytic formulas given in Sec. II, except for the determination of the phase ϕ, which must be estimated from a Kramers-Kronig analysis. A test of this procedure for Au is shown in Fig. 12. In this case the isolated first-shell EXAFS is compared with data from Au foil standard and excellent agreement is seen. The corrections are angle dependent, and the results for a wide range of incident angles are listed in Table I.

The values in Table I were determined by comparing the corrected and uncorrected first shells with the first shell in a Au foil standard using the ratio method.[1] The errors come from noise in the data and any nonlinear behavior of the amplitude ratios. Note that the errors tend to decrease after correction indicating a more linear ratio. These k-dependent contributions to the corrections are, however, fairly small, and their effect on determinations of the value of the Debye-Waller factor σ^2 is usually not important.

The corrected amplitudes are consistently less than 1. At low angles this could be due to a reduced amplitude from the surface layer. However, a similar trend continues to high angles where the surface contribution is

TABLE I. Comparison of the first-shell corrected and uncorrected amplitudes for the glancing-angle EXAFS obtained for pure Au at various incident angles. The critical angle for Au in the EXAFS energy range is about 6.6 mrad. The numbers in parentheses are the estimated errors in the last digit.

Angle (mrad)	Uncorrected amplitude	Corrected amplitude
3.12	0.90(3)	0.93(3)
4.15	0.90(3)	0.95(2)
5.17	0.86(5)	0.93(4)
6.20	0.74(4)	0.96(2)
7.23	0.41(3)	0.93(2)
8.25	0.33(4)	0.76(3)
9.28	0.41(4)	0.91(2)

small, indicating the discrepancy may be due to the correction. In any case 5% accuracy for the amplitude is a typical result for an EXAFS measurement even when standard techniques are used. The data taken at 8.25 mrad seem to contain an as yet undetermined experimental error since the result is inconsistent with the neighboring values.

Figure 12 also shows that the phase-shift distortion is well corrected. The phase distortion is somewhat k dependent and, in the worst case, near the critical angle would shift the distance determination by only 0.03 Å if uncorrected. Thus, correction of the phase is not as critical as the amplitude and the model is entirely satisfactory.

The corrections were also applied to the Cu/Al interface. In this case it is important to have a good model for the reflectivity data, as is shown in Fig. 7 for the sample evaporated at 10^{-6} Torr. Because the sputtered sample has such an extremely rough interface, it was not possible to obtain such a good fit to the reflectivity using existing models for roughness. Therefore, detailed quantitative analysis was not attempted for this sample.

Both of the evaporated samples were analyzed as for the Au data. The first-shell EXAFS contribution was isolated and corrected for anomalous dispersion. The results are shown in Figs. 13 and 14. Considering first the data from the non-UHV sample shown in Fig. 13, it is seen that the first-shell EXAFS is quite similar to Cu, but there are some systematic deviations. The amplitude is significantly reduced, and there is a phase mismatch at low k. The solid curve is a fit to the data using a linear combination of the Cu and $CuAl_2$ first shells. An excellent fit is obtained if the Cu Debye-Waller factor, σ^2, is increased by about 0.0015 Å^2. Other fits were also attempted, including some with an isolated Cu-Al shell (the first shell in $CuAl_2$ contains eight Al neighbors at 2.60 Å and two Cu neighbors at 2.44 Å). In this case the Cu-Cu distance consistently was found to be 2.56 Å (the bulk Cu value), while the Cu-Al distance always was fitted to 2.66±0.02 Å. The fit in this case was slightly better, but since the Cu-Al contribution is so small, the fits are not particularly sensitive to changes in the Cu-Al parameters. It does seem, however, that the Cu-Al contribution is quite similar to that in $CuAl_2$. The results are summarized in Table II.

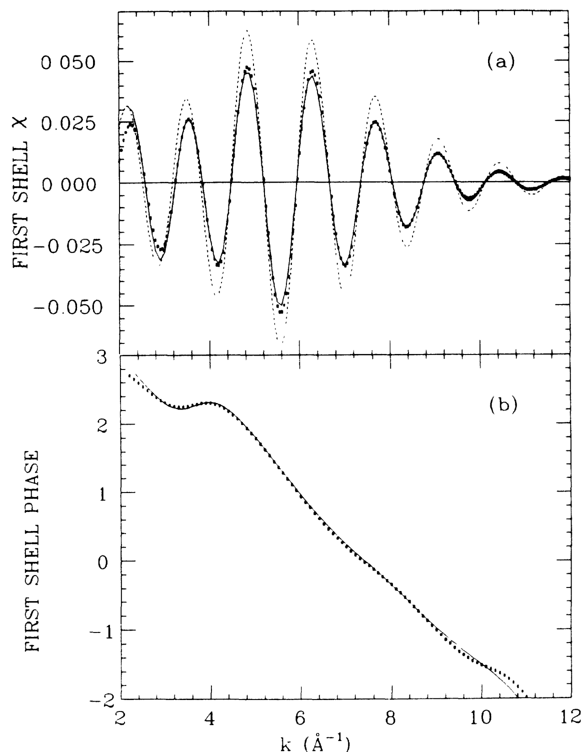

FIG. 13. Comparison of the fitted EXAFS spectrum (solid line) with the data (points) for the 10^{-6} Torr evaporated sample. The fitting parameters are given in Table II under Cu + $CuAl_2$. The pure Cu first shell is shown for comparison (dashed line).

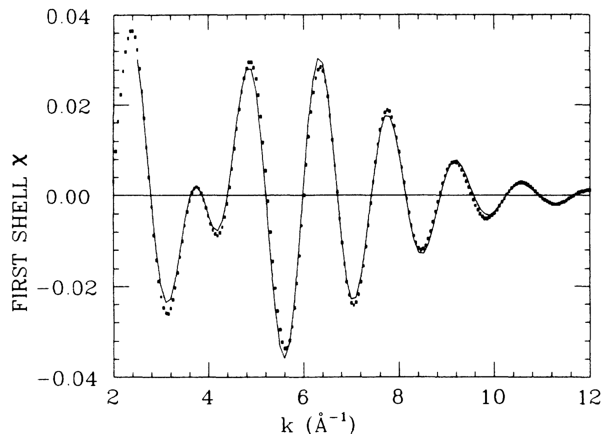

FIG. 14. Comparison of the fitted EXAFS spectrum (solid line) with the data (points) for the UHV sample. The fitting parameters are given in Table II.

Since the dominant change in the glancing-angle data is a reduction in the Cu amplitude, it is legitimate to ask if the effect could be due to an improper correction. A close look at the phase of the data, however, indicates that Cu—Al bonds are present. As shown in Fig. 13(b) there is a distinct interference in the phase near $k=4$ which cannot be due to the correction or distortion since they are both monotonic in this k range. This interference is well fitted by the addition of Cu—Al bonds.

For the data from the UHV-prepared sample similar interference is clearly seen in the isolated first-shell data. Again, fits were attempted using the Cu and $CuAl_2$ first shell, but in this case they were not successful. The Cu—Al bond length is definitely different from that in $CuAl_2$. We were, therefore, led to a fit which allows both the Cu-Cu and Cu-Al distances and amplitudes to vary. The results are shown in Fig. 14 and Table II. The Cu-Al distance is slightly smaller than its value in bulk $CuAl_2$. Again, the Cu-Cu σ^2 is increased over the bulk value. The addition of a second Cu—Cu bond at a shorter distance as is found in $CuAl_2$ did not significantly improve the fits.

The coordination numbers in Table II are divided by the bulk values for Cu and $CuAl_2$. If the contributions are due to separate Cu- and $CuAl_2$-like regions, the values would then represent the fractional contribution to the signal of each region. The fact that the sum of the Cu-Cu and Cu-Al values is very close to 1 lends support to this interpretation. Then, from penetration-depth calculations similar to those in Fig. 4, the equivalent thickness of the Cu-Al region can be estimated. For an ideal interface the values are ~12 Å for the non-UHV case and ~37 Å for the UHV sample. To first order the observed roughness should not significantly increase these values since they are based on the ratio of Cu-Al to Cu-Cu signals. Simple roughness would increase both signals by similar amounts.

The finding that the Cu-Al distance is different for the two samples may indicate two types of Cu-Al regions are present in the samples. For the non-UHV sample there may be little reaction at the interface with the bulk of the Cu-Al signal coming from dilute Cu in the Al layer, as in-

TABLE II. Fitting results for the first-shell data shown in Figs. 13 and 14. The coordination numbers N are divided by 12 and 8 for the Cu-Cu and Cu-Al contributions, respectively, since these are the corresponding values for bulk Cu and $CuAl_2$. The fitting with $CuAl_2$ includes the Cu-Cu shell found at 2.44 Å in $CuAl_2$. For the other fits this contribution was removed.

	Cu-Cu			Cu-Al	
Fit	$N/12$	R (Å)	$\Delta\sigma^2$ (Å^2)	$N/8$	R (Å)
Non-UHV					
Cu + $CuAl_2$	0.88±0.03	2.56±0.01	0.0015±0.0005	0.10±0.03	2.60 (fixed)
Cu + Cu-Al	0.87±0.03	2.56±0.01	0.0015±0.0005	0.10±0.03	2.66±0.02
UHV					
Cu + Cu-Al	0.73±0.02	2.56±0.01	0.0028±0.0005	0.29±0.03	2.56±0.01

dicated by the reflectivity fits. For the UHV samples the results may be more indicative of a reacted Cu-Al layer that is seen to exist at the interface in the angle-dependent results of Fig. 11. The Cu-Cu results lend support for the above supposition. The Cu—Cu disorder is larger for the UHV sample, where there is more interfacial reaction. This may be due to a concentration gradient causing strain in the Cu near the interface. It should be noted that large-angle data which measured the entire Cu layer gave results identical to those of bulk Cu. Therefore, only the interfacial Cu is being changed.

VIII. CONCLUSIONS

The results presented clearly show the value of glancing-angle EXAFS measurements for studying interfacial regions. The main features of the technique have been demonstrated, including interface sensitivity, element specificity, and controllable penetration depth. The Cu-Al results provide a clear example of the types of information which glancing-angle EXAFS measurements can provide. The distortions to the EXAFS spectra are a problem, but can be dealt with both experimentally and in the analysis procedures. A key component to a successful glancing-angle experiment are accurate reflectivity measurements. These are required for accurate calculation of EXAFS distortion corrections, and, as shown, can provide useful information of the thin-film morphology.

It is interesting to compare EXAFS and reflectivity measurements with other techniques for characterizing interfaces. High-resolution transmission electron microscopy (TEM) has proven to be an extremely powerful tool for characterizing interfaces, as the photos in Fig. 6 illustrate, and on epitaxial interfaces lattice-imaging techniques can provide even more detail. However, sample preparation is destructive and difficult, and it is legitimate to ask how representative the prepared sample is of the original interface after such extensive preparation. Also, EXAFS can provide bonding information to 0.01 Å even in disordered systems, a capability which TEM lacks.

Two other techniques widely used are depth profiling by sputtering and Auger analysis, and Rutherford backscattering (RBS). Both provide compositional information, but do not directly determine structural parameters. These must be inferred from the compositional dependence or determined by other techniques. RBS is an easy-to-apply nondestructive technique, and has found wide application is annealing studies of thin films. However, in most cases the depth resolution for buried interfaces is 50–100 Å. Sputter techniques have to contend with problems of differential sputtering.

Structural information can be obtained by glancing-angle x-ray diffraction. When used in conjunction with RBS, as for the Cu/Al case,[19,20] a fairly complete picture of the interface evolution can often be derived. The sensitivity of laboratory-based diffraction instruments usually requires ~ 100 Å layers for clear identification. This sensitivity may be improved for synchrotron experiments, but it is still difficult to separate the interface and bulk components for buried interfaces. In EXAFS this is done by tuning to a particular absorption edge, while for diffraction more complex anomalous scattering experiments are required. Also, disordered or amorphous interfaces will remain very difficult to detect by any diffraction technique.

Thus, no interface technique is definitive and a combination is usually required for a complete structural determination. This paper has shown how EXAFS and reflectivity measurements can provide unique structural information, and, when combined with more traditional methods, they should make important contributions to interface studies.

ACKNOWLEDGMENTS

We would like to thank R. DiNardo for preparing the samples and J. Tafto, R. Sabatini, R. Corderman, and A. Hanson for their help in characterizing the samples. This work was supported by the U.S. Department of Energy (Division of Materials Science) under Contract Nos. DE-AS05-80ER10742 and DE-AC02-76CH00016.

[1]E. A. Stern and S. M. Heald, in *Handbook of Synchrotron Radiation*, edited by E. E. Koch (North-Holland, Amsterdam, 1983), Vol. 1b, p. 955.

[2]S. M. Heald, J. M. Tranquada, B. M. Clemens, and J. P. Stec, J. Phys. (Paris) Colloq. **47**, C8-1061 (1986).

[3]L. G. Parratt, Phys. Rev. **95**, 359 (1954).

[4]R. Barchewitz, M. Cremonse-Visicato, and G. Onori, J. Phys C **11**, 4439 (1978).

[5]G. Martens and P. Rabe, Phys. Status Solidi A **58**, 415 (1980).

[6]R. Fox and S. J. Gurman, J. Phys. C **13**, L249 (1980).

[7]L. Bosio, R. Cortes, A. Defrain, and M. Froment, J. Electroanal. Chem. **180**, 265 (1984).

[8]S. M. Heald, E. Keller, and E. A. Stern, Phys. Lett. **103A**, 155 (1984).

[9]S. M. Heald, J. M. Tranquada, D. O. Welch, and H. Chen, Mater. Res. Soc. Symp. Proc. **37**, 437 (1985).

[10]S. M. Heald, H. Chen, and J. M. Tranquada, Mater. Res. Soc. Symp. Proc. **54**, 165 (1986).

[11]S. M. Heald, J. M. Tranquada, and H. Chen, J. Phys. (Paris) Colloq. **47**, C8-825 (1986).

[12]A good general reference for this section is R. W. James, *The Optical Principles of the Diffraction of X-rays* (Bell, London, 1958). See also L. G. Parratt and C. F. Hempstead, Phys. Rev. **94**, 1593 (1954).

[13]D. T. Cromer and D. Liberman, Acta. Crystallogr. Sect. A **37**, 267 (1981).

[14]D. T. Cromer, J. Appl. Crystallogr. **16**, 437 (1983).

[15]U. Bonse, I. Hartmann-Lotsch, H. Lotsch, in *EXAFS and Near Edge Structure*, edited by A. Bianconi, L. Incoccia, and S. Stipcich (Springer-Verlag, Berlin, 1983), p. 376.

[16]P. Dreier, P. Rabe, W. Malzfeldt, and W. Niemann, in *EXAFS and Near Edge Structure*, Ref. 15, p. 378.

[17]B. Vidal and P. Vincent, Appl. Opt. **23**, 1794 (1984).
[18]See, for example, E. L. Church, SPIE Proc. **184**, 196 (1979), or J. M. Elson and J. M. Bennett, Opt. Eng. **18**, 116 (1979).
[19]R. A. Hamm and J. M. Vandenberg, J. Appl. Phys. **56**, 293 (1984).
[20]H. T. G. Hentzell, R. D. Thompson, and K. N. Tu, J. Appl. Phys. **54**, 6923 (1983).

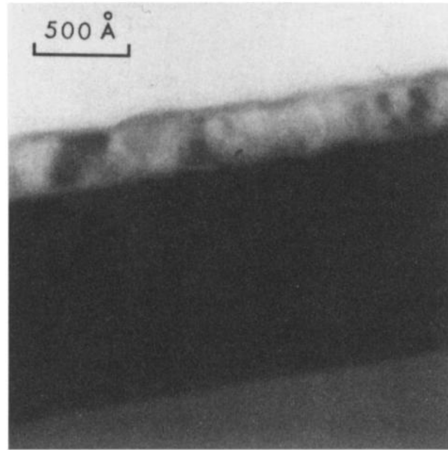

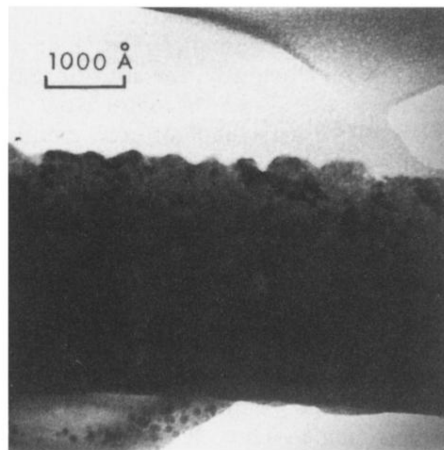

FIG. 6. Cross-sectional TEM photographs of (a) evaporated Al/Cu bilayer, and (b) sputtered Al/Cu bilayer.